



**HAL**  
open science

## Phase transition boundary between fcc and hcp structures in Fe-Si alloy and its implications for terrestrial planetary cores

Tetsuya Komabayashi, Giacomo Pesce, Guillaume Morard, Daniele Antonangeli, Ryosuke Sinmyo, Mohamed Mezouar

### ► To cite this version:

Tetsuya Komabayashi, Giacomo Pesce, Guillaume Morard, Daniele Antonangeli, Ryosuke Sinmyo, et al.. Phase transition boundary between fcc and hcp structures in Fe-Si alloy and its implications for terrestrial planetary cores. *The American Mineralogist*, 2019, 104 (1), pp.94-99. 10.2138/am-2019-6636. hal-02104726

**HAL Id: hal-02104726**

**<https://hal.science/hal-02104726>**

Submitted on 27 Nov 2020

**HAL** is a multi-disciplinary open access archive for the deposit and dissemination of scientific research documents, whether they are published or not. The documents may come from teaching and research institutions in France or abroad, or from public or private research centers.

L'archive ouverte pluridisciplinaire **HAL**, est destinée au dépôt et à la diffusion de documents scientifiques de niveau recherche, publiés ou non, émanant des établissements d'enseignement et de recherche français ou étrangers, des laboratoires publics ou privés.



THE UNIVERSITY *of* EDINBURGH

Edinburgh Research Explorer

## Phase transition boundary between fcc and hcp structures in Fe-Si alloy and its implications for terrestrial planetary cores

### Citation for published version:

Komabayashi, T, Pesce, G, Morard, G, Antonangeli, D, Sinmyo, R & Mezouar, M 2019, 'Phase transition boundary between fcc and hcp structures in Fe-Si alloy and its implications for terrestrial planetary cores', *American Mineralogist*, vol. 104, no. 1, pp. 94-99. <https://doi.org/10.2138/am-2019-6636>

### Digital Object Identifier (DOI):

[10.2138/am-2019-6636](https://doi.org/10.2138/am-2019-6636)

### Link:

[Link to publication record in Edinburgh Research Explorer](#)

### Document Version:

Peer reviewed version

### Published In:

American Mineralogist

### General rights

Copyright for the publications made accessible via the Edinburgh Research Explorer is retained by the author(s) and / or other copyright owners and it is a condition of accessing these publications that users recognise and abide by the legal requirements associated with these rights.

### Take down policy

The University of Edinburgh has made every reasonable effort to ensure that Edinburgh Research Explorer content complies with UK legislation. If you believe that the public display of this file breaches copyright please contact [openaccess@ed.ac.uk](mailto:openaccess@ed.ac.uk) providing details, and we will remove access to the work immediately and investigate your claim.



## Revision 2

# Phase transition boundary between fcc and hcp structures in Fe-Si alloy and its implications for terrestrial planetary cores

Tetsuya Komabayashi<sup>1\*</sup>, Giacomo Pesce<sup>1</sup>, Guillaume Morard<sup>2</sup>, Daniele Antonangeli<sup>2</sup>, Ryosuke Sinmyo<sup>3†</sup>, Mohamed Mezouar<sup>4</sup>

<sup>1</sup>School of GeoSciences and Centre for Science at Extreme Conditions, University of Edinburgh EH9 3FE, UK

<sup>2</sup>Sorbonne Université, Muséum National d'Histoire Naturelle, UMR CNRS 7590, IRD, Institut de Minéralogie, de Physique des Matériaux et de Cosmochimie, IMPMC, 75005 Paris, France

<sup>3</sup>Bayerisches Geoinstitut, Universitat Bayreuth, 95440 Bayreuth, Germany

<sup>4</sup>European Synchrotron Radiation Facility, BP 220, F-38043 Grenoble Cedex, France

\*corresponding author: Tetsuya Komabayashi

E-mail: [tetsuya.komabayashi@ed.ac.uk](mailto:tetsuya.komabayashi@ed.ac.uk)

†Now at Department of Earth and Planetary Science, University of Tokyo, 7-3-1 Hongo, Bunkyo, Tokyo 113-0033, Japan

## ABSTRACT

1  
2 The phase transition between a face-centered cubic (fcc) and hexagonal close-packed  
3 (hcp) structures in Fe-4wt% Si alloy was examined in an internally resistive heated  
4 diamond anvil cell (DAC) under high-pressure ( $P$ ) and -temperature ( $T$ ) conditions to  
5 71 GPa and 2000 K by *in-situ* synchrotron X-ray diffraction. Complementary  
6 laser-heated DAC experiments were performed in Fe-6.5wt% Si. The fcc-hcp phase  
7 transition boundaries in the Fe-Si alloys are located at higher temperatures than that in  
8 pure Fe, indicating that the addition of Si expands the hcp stability field. The  $dP/dT$   
9 slope of the boundary of the entrant fcc phase in Fe-4wt% Si is similar to that of pure Fe,  
10 but the two-phases region is observed over a temperature range increasing with pressure,  
11 going from 50 K at 15 GPa to 150 K at 40 GPa. The triple point, where the fcc, hcp, and  
12 liquid phases coexist in Fe-4wt% Si, is placed at 90-105 GPa and 3300-3600 K with the  
13 melting curve same as in Fe is assumed. This supports the idea that the hcp phase is  
14 stable at Earth's inner core conditions. The stable structures of the inner cores of the  
15 other terrestrial planets are also discussed based on their P-T conditions relative to the  
16 triple point. In view of the reduced P-T conditions of the core of Mercury (well below  
17 the triple point), an Fe-Si alloy with a Si content up to 6.5 wt% would likely crystallize  
18 an inner core with an fcc structure. Both Venusian and Martian cores are believed to

19 currently be totally molten. Upon secular cooling, Venus is expected to crystallize an  
20 inner core with an hcp structure, as the pressures are similar to those of the Earth's core  
21 (far beyond the triple point). Martian inner core will take an hcp or fcc structure  
22 depending on the actual Si content and temperature.

23

#### 24 **Key words**

25 Earth's core; high-pressure; diamond anvil cell; internal resistive heating; Fe-Si alloy

26

27

## INTRODUCTION

28 Terrestrial core formation process has been discussed in relation to  
29 metal-silicate equilibration during accretion stage (Li and Agee 1996; Wade and Wood  
30 2005; Siebert et al. 2013) although some recent models considered disequilibrium  
31 processes at a later stage (Rubie et al. 2011). The metal-silicate equilibration inevitably  
32 results in an impure iron rich metallic core (Wade and Wood; Siebert et al. 2013). The  
33 impurity includes nickel and several less dense elements which are also called light  
34 elements (Poirier 1994; Allègre et al. 1995).

35 Birch (1952) pointed out that the density of pure iron might be greater than the  
36 seismological determination for Earth's core. Such a density deficit has been associated

37 with the presence of lighter element(s), and a recent internally consistent  
38 thermodynamic model of pure iron estimated the core density deficit to be 7% for the  
39 outer core and 4.5 % for the inner core (Komabayashi 2014). Other terrestrial planetary  
40 cores also likely contain light elements considering metal-silicate partitioning during  
41 their cores formation. In addition, the presence of a magnetic field found in some  
42 terrestrial planets may indicate the presence of a light element-bearing partially molten  
43 core (e.g., Sohl and Schubert 2007). Light elements would be expelled at the bottom of  
44 the liquid outer core as it is less partitioned in the solid inner core and this would drive  
45 convection in the outer core (Stevenson et al. 1983; Lister and Buffett 1995).

46         Among the potential light elements, silicon is considered a plausible candidate  
47 for the terrestrial planetary cores for various reasons: i) silicon is the second most  
48 abundant element in the mantle and series of high-pressure (P) and –temperature (T)  
49 experiments demonstrated that silicon and oxygen could be dissolved from mantle  
50 silicates to core melt (Takafuji et al. 2005; Ozawa et al. 2009), and then silicon is  
51 partitioned between solid and liquid during core crystallization; ii) silicon isotopic  
52 composition of stony meteorites is different from bulk silicate Earth (Georg et al. 2007;  
53 Fitoussi et al. 2009), implying that silicon might have been partitioned into the core  
54 during core-mantle differentiation (Shahar et al. 2011; Hin et al. 2014); iii) all the core

55 formation models based on silicate-metal equilibration inevitably have silicon as a light  
56 element in the core (Wade and Wood 2005; Rubie et al. 2011; Siebert et al. 2013).

57 Phase relations and equations of state (EoS) of solid phases in the system  
58 Fe-(Fe)Si have been extensively studied by both experiment and theory (Alfe et al.  
59 2002; Dobson et al. 2002; Lin et al. 2002; Kuwayama and Hirose 2004; Lin et al. 2009;  
60 Tateno et al. 2015; Ozawa et al. 2016). An important phase relation is the transition  
61 between face-centered cubic (fcc) and hexagonal close-packed (hcp) structures, as this  
62 is central to address the solid inner core structure (Uchida et al. 2001; Asanuma et al.  
63 2008; Komabayashi et al. 2009), and the P-T location of the phase boundary can be  
64 used to deduce thermodynamic properties (Wood 1993; Komabayashi 2014). Notably,  
65 the triple point P-T location where the hcp, fcc, and liquid phases coexist can be  
66 constrained from the fcc-hcp boundary and melting curve (Zhang et al. 2016). An  
67 experimental study in a laser-heated diamond anvil cell (DAC) reported that the  
68 transition temperature was greatly reduced when 3.4 wt%Si was added to Fe (Asanuma  
69 et al. 2008). In contrast, phase relations inferred by Fischer et al. (2013) suggested that  
70 addition of silicon should increase the transition temperature. Tateno et al. (2015)  
71 experimentally demonstrated that the transition temperature was increased by the  
72 addition of 6.5 wt%Si to iron. As such the effect of Si on the transition temperature has

73 been a controversy and the P-T conditions of the actual boundaries in the system Fe-Si  
74 are not unanimous.

75 In this study, we present the investigation of the P-T locations of the fcc-hcp  
76 transition boundaries in Fe-Si alloys in an internally resistive heated DAC. The  
77 internally heated DAC heats the sample by its resistance, with an improved accuracy in  
78 temperature with respect to conventional laser heated DAC (Komabayashi et al. 2009;  
79 2012). Based on these experimental results, we will discuss the effect of Si on the Fe  
80 properties under high P-T condition and address the stable structure of a solid Fe-Si  
81 alloy at the conditions of the inner cores of the terrestrial planets of the solar system.

82

## 83 **EXPERIMENTAL PROCEDURE**

84 We conducted high-P-T in-situ X-ray diffraction (XRD) experiments on Fe-Si  
85 samples at the beamline ID27, European Synchrotron Radiation Facility (ESRF). X-rays  
86 with a wavelength of  $0.3738\text{\AA}$  were focused to a  $3\times 3\ \mu\text{m}^2$  spot at sample position and  
87 the diffracted X-rays were collected on a two dimensional detector (mar345 Image Plate  
88 Detector). The collection time was 10 seconds for each measurement. Using the fit-2D  
89 program (Hammersley 1996), the obtained data were converted to the conventional  
90 one-dimensional XRD pattern.



91 High pressure was generated in a DAC with a pair of diamond anvils with a  
92 culet size of 300  $\mu\text{m}$  or 150-450  $\mu\text{m}$  beveled depending on the pressure range. The  
93 starting material was a 5-7  $\mu\text{m}$  thick Fe-Si alloy with 4 wt% Si (Rare Metallic. Co.,  
94 hereafter Fe-4Si), placed in the sample chamber and connected to platinum leads. The  
95 junction between the Fe sample and Pt leads was outside the sample chamber (see  
96 Komabayashi et al. (2009) for the sample geometry).  $\text{SiO}_2$  glass layers served as a  
97 pressure transmitting medium and thermal insulator. High temperature was achieved  
98 with an internal resistive system (Komabayashi et al. 2009; 2012; Antonangeli et al.  
99 2012). The sample was resistively heated by directly applying a DC voltage by an  
100 external power supply. The temperature was measured by a spectral radiometric system  
101 as conventional in laser heating experiments. Noteworthy, thanks to the improved time  
102 and spatial stability of the hotspot and the reduced thermal gradients, resulting  
103 uncertainties in temperature were about 50 K (Komabayashi et al., 2012)

104 Complementary laser heating experiments were conducted on an Fe-6.5Si  
105 sample (Rare Metallic. Co.) at ID27, ESRF (see Morard et al. (2011) for details of the  
106 laser heating experimental set up). The internal heating system was not applied because  
107 this alloy is so brittle that it was not possible to make it into thin foil. Irrespectively of  
108 the use of low numerical aperture and reflecting objectives which effectively minimize

109 the chromatic aberration and improve reliability of temperature determination (Mezouar  
110 et al. 2017), the laser heating experiments show larger temperature uncertainty due to  
111 large temperature gradient across the sample and laser fluctuations. The two microns  
112 diameter pinhole at the entrance of the spectrometer allows for a collection of signal  
113 only coming from the very central part of the hotspot and an optimal alignment of lasers  
114 and X-ray beam. Morard et al. (2011) discussed that the possible uncertainty in the  
115 temperature in this experimental setup might be 150 K at 3000 K. In the present study,  
116 we assumed a more conservative number, 10% of the generated temperature.

117 In all the runs, the pressure at any given temperature was calculated with a  
118 thermal EoS for Fe-4Si or Fe-6.5Si with the hcp structure that was assessed based on  
119 pure iron (Dewaele et al. 2006) and Fe-9wt%Si (Tateno et al. 2015). The room  
120 temperature parameters for the Vinet EoS were obtained by averaging on the basis of  
121 mole fraction between the two compositions: for Fe-4Si,  $V_0 = 22.56 \text{ \AA}^3$ ,  $K_0 = 166 \text{ GPa}$ ,  
122  $K' = 5.4$ , and for Fe-6.5Si,  $V_0 = 22.63 \text{ \AA}^3$ ,  $K_0 = 167 \text{ GPa}$ ,  $K' = 5.5$ , where  $V_0$ ,  $K_0$ ,  $K'$  are  
123 the unit-cell volume, bulk modulus, and its pressure derivative at 300 K and 1 bar,  
124 respectively. We assumed the same thermal parameters as for pure iron (Dewaele et al.  
125 2006; Tateno et al. 2015).

126 The thermal pressure effect on the sample pressure was checked against the

127 pressure for the SiO<sub>2</sub> pressure medium. The EoS for stishovite by Wang et al (2012) was  
128 used to calculate the pressure for SiO<sub>2</sub>. As the precise temperature for the pressure  
129 medium was unknown, we calculated the pressure for SiO<sub>2</sub> at the sample temperature  
130 and 300 K. At 42.8 GPa and 1940 K for the sample, the pressure for SiO<sub>2</sub> were 44.9  
131 GPa and 34.1 GPa at 1940 K and 300 K respectively. Since the crystallized portion of  
132 the pressure medium should be at the same (or slightly lower) temperature of the sample,  
133 the above calculation independently supports our pressure determination for the iron  
134 alloy. Also, after quench, the pressure for SiO<sub>2</sub> is  $37.6 \pm 1.0$  GPa, which is consistent  
135 with the sample pressure of  $36.6 \pm 0.4$  GPa. Therefore, we can conclude that the  
136 pressure estimation at high temperatures is reasonable.

137         The use of the unit-cell volume of the hcp phase in the pressure calculation  
138 may introduce an uncertainty when the experimental condition is near the completion of  
139 the hcp-fcc reaction. Based on a binary temperature-composition (T-X) phase loop  
140 detailed below, the pressure could have been underestimated by less than 1.3 GPa at 40  
141 GPa and 1870K. When the unit-cell volume for the hcp phase was not obtained, due to  
142 either grain growth or complete transition to the fcc phase, we assumed constant  
143 pressure upon further heating.

144

## RESULTS

145

### 146 **Fe-4Si**

147 Six separate in-situ XRD experiments were carried out on the Fe-4Si sample in  
148 the internally heated DAC. The results are illustrated in Fig. 1a and summarized in  
149 Table 1.

150 In the first run, the sample was compressed to 16.4 GPa and the XRD pattern  
151 shows coexistence of the bcc and hcp phases. Then the sample was heated to 1060 K  
152 and the fcc phase, with a minor amount of hcp phase, was observed. The hcp phase  
153 disappeared in the following XRD pattern at a similar temperature of 1050 K.  
154 Temperature slightly increased with time to 1080 K at steady power from the DC power  
155 supply without further changes in the pattern. Then, we tried to reverse the reaction. As  
156 the spectroradiometric method could not reliably measure temperatures below 1000 K,  
157 the temperature was estimated based on the linear power-temperature relationship  
158 established at 1060 K. During the cooling path, the reversal reaction started at 860 K,  
159 200 K lower than the reaction in the forward heating cycle. Further decreasing  
160 temperature to 770 K only slightly promoted the reaction, which suggests that  
161 nucleation of the hcp phase is very sluggish and implies that the width of the reaction in  
162 the backward cycle is much wider than the forward cycle. Accordingly, we constrained

163 the P-T conditions of the reaction in the forward cycle only and the results of the  
164 backward cycle are not listed in Table 1 to avoid confusion.

165 In the following runs, we only employed heating cycles which started from the  
166 hcp phase towards the fcc stability field. In the runs 2, 3, and 4, we observed a transition  
167 sequence from hcp to hcp+fcc and to fcc with increasing temperature. Figure 2 shows a  
168 series of XRD patterns collected during the run 2 for increasing temperature at about 24  
169 GPa. The temperature was first held at 1120 K for 4 minutes, observing only the hcp  
170 phase. Then we increased the temperature to 1230 K and fcc peaks appeared. No further  
171 changes in the XRD pattern were recognized during the following 40 minutes, during  
172 which the temperature was kept constant. We further increased the temperature to 1260  
173 K, which instantaneously increased the intensity of the fcc peaks. During the following  
174 30 minutes at constant temperature, the XRD patterns did not show significant changes.  
175 The transition was completed at 1330 K. In summary, the drastic changes in XRD were  
176 observed only upon temperature increase. The transition from the hcp to fcc phase  
177 seems to be very fast, with minimal kinetic effects.

178 In the runs 5 and 6, we observed no structural change to the highest  
179 temperatures and confirmed stability of the hcp phase to 71.0 GPa and 2020 K.

180 Overall, thanks to the performances of the internal heating system, we have

181 been able to place tight constraints on the P-T location of the transition boundaries. In  
182 particular, the width of the phase loop was accurately constrained. The  $dP/dT$  slope of  
183 the boundary of the entrant fcc phase in Fe-4wt% Si is similar to that of pure Fe, while  
184 the temperature interval of the two-phase region expands with increasing pressure from  
185 50 K at 15 GPa to 150 K at 40 GPa (Fig. 1a).

186

### 187 **Fe-6.5Si**

188 Two separate laser-heating runs were conducted on the Fe-6.5Si sample (Fig.  
189 1b). Same as for the internal-heating runs, we increased the temperature under high  
190 pressures. In the first run, we compressed the sample to 24.0 GPa at room temperature  
191 and then heated it by laser, reporting the appearance of fcc peaks at 1850 K in  
192 coexistence with hcp peaks. In the second run, we observed a complete transition to the  
193 fcc phase at 2340 K and 56.6 GPa. Considering the uncertainty in temperature in the  
194 laser heating experiment (i.e.,  $\pm 10\%$ ), the present experimental data are consistent with  
195 results by Tateno et al. (2015) (Fig. 1b).

196

197

## **DISCUSSION**

198 **Effect of Si on the fcc-hcp transition**

199           The present experiments confirmed the enlarged high temperature stability of  
200 the hcp phase in Fe-4Si and Fe-6.5Si with respect to the case in pure Fe (Fig. 1), in  
201 agreement with Fischer et al. (2013) and Tateno et al. (2015) but in contrast to Asanuma  
202 et al. (2008). Dissecting the XRD patterns in Asanuma et al. (2008), we noted that they  
203 assigned tiny shallow rises as peaks from the fcc phase, while the appearance of the fcc  
204 phase is clearly marked by the presence of the (200) peak (Fig. 2) (Komabayashi et al.  
205 2009; 2012). We conclude that the transition temperature between the hcp and fcc  
206 phases increases with Si content.

207           Figure 3 shows a T-X diagram at 40 GPa based on the present data on Fe-4Si  
208 and Fe-6.5Si and existing experimental data on pure Fe and Fe-9Si (Komabayashi et al.  
209 2009; Tateno et al. 2015). The fcc-hcp transition temperature increases with Si content.  
210 The P-T conditions for a reaction  $hcp = hcp + B2$  phase (Tateno et al. 2015) placed  
211 additional constraint on the phase diagram (Fig. 3). The maximum solubility of Si into  
212 the fcc phase should be about 7 wt%. A thermodynamic model will be made to fit the  
213 data in the near future.

214

215

## IMPLICATIONS

216           Figure 4 shows a phase diagram of iron alloys reporting the fcc-hcp boundaries

217 in Fe, Fe-4Si, and Fe-6.5Si, together with the P-T ranges for the cores of Mars and  
218 Mercury. Addition of Si to Fe expands the stability of the hcp phase as confirmed by the  
219 P-T locations of the fcc-hcp transitions observed in this study, which are consistent with  
220 Tateno et al. (2015) based on a laser-heated DAC experiments (Fig. 1b). The triple point  
221 where the fcc, hcp, and liquid phases coexist in Fe-4wt% Si is placed at 90-105 GPa and  
222 3300-3600 K (the melting curve is assumed to be the same as in Fe as Si inclusion at  
223 4wt% level should not significantly affect the melting temperature (Morard et al. 2011)),  
224 supporting the idea that Earth's inner core at 330-364 GPa is made up with the hcp  
225 phase. Tateno et al. (2015) similarly proposed that the inner core would be made of a  
226 sole hcp alloy if the Si content is up to 7 wt.%.

227 More complex can be the cases for the other terrestrial planets of the solar  
228 system, namely, Venus, Mercury, and Mars. Due to the lack of seismic data,  
229 information about their internal structures heavily depends on the average density. As  
230 such, the core density deficit cannot be pertinently discussed. Nevertheless geophysical  
231 modelling studies argued for the presence of light elements in the cores and kept this  
232 into consideration when simulating planetary core, and in particular when discussing  
233 their molten/solid state (Stevenson et al. 1983; Williams and Nimmo 2004; Rivoldini et  
234 al. 2011; Dumberry and Rivoldini 2015; Knibbe and van Westrenen 2018). In the



235 following, we will limit our discussion to the Fe-Si-S system. Tsujino et al. (2013)  
236 summarized existing thermal models for terrestrial core-mantle boundaries in the  
237 system Fe-S (Stevenson et al. 1983; Sohl and Spohn 1997; Fei et al. 2000; Williams and  
238 Nimmo 2004) and assessed the adiabats across the cores on the basis of the Grüneisen  
239 parameter for pure fcc iron (Fig. 4). The known reduction of the crystallizing  
240 temperature of iron by addition of silicon (Kubaschewski 1993; Kuwayama and Hirose  
241 2004) implies that the thermal profiles in Fig. 4, which are based on the liquidus of the  
242 system Fe-S, can be considered as the maximum estimates for the system Fe-Si-S.

243 Venus' similar size to the Earth implies that its internal structure is  
244 differentiated into crust, mantle, and core (Sohl and Schubert 2007). However,  
245 contrarily to the Earth, Venus does not have a global magnetic field. The pressure at the  
246 center of the planet was estimated to be 295 GPa which is slightly lower than of the  
247 Earth and crystallization of the liquid core might have not yet started (Stevenson et al.  
248 1983). Since the core pressure is far greater than the triple point pressure in the system  
249 Fe-4Si (Fig. 4), when upon secular cooling the inner core will start crystallizing,  
250 likewise the Earth, it should take an hcp phase.

251 It is suggested that Mercury has a partially molten iron core as it shows a  
252 dipole magnetic field from a spacecraft observation (Ness 1979). Further support of the

253 presence of a liquid portion of the core comes from and the amplitude of its librations  
254 (Margot et al. 2005). The suggested thermal structure of Mercurian core modeled on the  
255 basis of the system Fe-S argues for a temperature much higher than the fcc-hcp  
256 transition in Fe-6.5Si (Fig. 4). Recently proposed thermal models of Fe-Si cores showed  
257 a similar temperature range as in Fig. 4 (Knibbe and van Westrenen 2018). Hence  
258 Mercurian inner core is expected to take an fcc structure if the Si content is less than 6.5  
259 wt%. Only upon further cooling, the fcc-structured alloy in Mercurian inner core, will  
260 be transformed to the hcp phase.

261           Mars currently does not have an active global magnetic field, although it has a  
262 metallic core in view of its average density and moment of inertia (Yoder et al. 2003).  
263 However, the presence of magnetized rock records found in southern highland area  
264 indicates that the planet should have had a magnetic field in the past. Stevenson et al.  
265 (1983) suggested that present Martian core should still be totally molten to account for  
266 the absence of the magnetic field and the rocks were magnetized by a field produced by  
267 a past, now extinct, thermal convection of the liquid core. The inferred thermal profiles  
268 of the core partially overlap with the fcc-hcp transition in Fe-4Si (Fig. 4). As such the  
269 first iron alloy crystal that will crystallize in the future will be either fcc or hcp phase  
270 depending on the actual Si content and exact temperature. In the case of the fcc phase, it

271 will be transformed to the hcp phase as the core further cools down.

272           In summary, the inner core structure of the terrestrial planets can be discussed  
273 based on the phase relations in Fig. 4. The hcp core would show more anisotropic  
274 seismic properties (Steinle-Neumann et al., 2001) than the fcc core because of the  
275 anisotropic crystal structure. Also the hcp core would be denser than the fcc core as the  
276 fcc-hcp transition in Fe-4Si shows about 0.8% density jump. Those changes are  
277 important in future attempts to construct a precise density model for the planetary  
278 interior.

279

280

## 281 **Acknowledgements**

282 The synchrotron experiments were performed at ID27 ESRF. This research was  
283 supported by the European Research Council (ERC) Consolidator Grant to TK (Earth  
284 core #647723).

285

286 **References**

- 287 Alfè, D., Gillan, M.J., and Price, G.D. (2002) Composition and temperature of the  
288 Earth's core constrained by combining ab initio calculations and seismic data.  
289 Earth and Planetary Science Letters 195, 91-98.
- 290 Allègre, C.J., Poirier, J.P., Humler, E., and Hofmann, A.W. (1995) The chemical  
291 composition of the Earth. Earth and Planetary Science Letters 134, 515-526.
- 292 Anderson, J.D., Colombo, G., Esposito, P.B., Lau, E.L., and Trager, G.B. (1987) The  
293 Mass, Gravity-Field, and Ephemeris of Mercury. Icarus 71, 337-349.
- 294 Antonangeli, D., Komabayashi, T., Ocelli, F., Borissenko, E., Walters, A.C., Fiquet, G.,  
295 and Fei, Y.W. (2012) Simultaneous sound velocity and density measurements of  
296 hcp iron up to 93 GPa and 1100 K: An experimental test of the Birch's law at  
297 high temperature. Earth and Planetary Science Letters 331, 210-214.
- 298 Asanuma, H., Ohtani, E., Sakai, T., Terasaki, H., Kamada, S., Hirao, N., Sata, N., and  
299 Ohishi, Y. (2008) Phase relations of Fe-Si alloy up to core conditions:  
300 Implications for the Earth inner core. Geophysical Research Letters 35, L12307,  
301 doi:10.1029/2008GL033863.
- 302 Birch, F. (1952) Elasticity and constitution of the Earth's interior. Journal of  
303 Geophysical Research 57, 227-286.

304 Dewaele, A., Loubeyre, P., Occelli, F., Mezouar, M., Dorogokupets, P.I., and Torrent, M.  
305 (2006) Quasihydrostatic equation of state of iron above 2 Mbar. *Physical Review*  
306 *Letters* 97, 215504.

307 Dobson, D.P., Vocadlo, L., and Wood, I.G. (2002) A new high-pressure phase of FeSi.  
308 *American Mineralogist* 87, 784-787.

309 Dumberry, M., Rivoldini, A. (2015) Mercury's inner core size and core-crystallization  
310 regime. *Icarus* 248, 254–268.

311 Fei, Y.W., Li, J., Bertka, C.M., and Prewitt, C.T. (2000) Structure type and bulk  
312 modulus of Fe<sub>3</sub>S, a new iron-sulfur compound. *American Mineralogist* 85,  
313 1830-1833.

314 Fischer, R.A., Campbell, A.J., Reaman, D.M., Miller, N.A., Heinz, D.L., Dera, P., and  
315 Prakapenka, V.B. (2013) Phase relations in the Fe-FeSi system at high pressures  
316 and temperatures. *Earth and Planetary Science Letters* 373, 54-64.

317 Fitoussi, C., Bourdon, B., Kleine, T., Oberli, F., and Reynolds, B.C. (2009) Si isotope  
318 systematics of meteorites and terrestrial peridotites: implications for Mg/Si  
319 fractionation in the solar nebula and for Si in the Earth's core. *Earth and*  
320 *Planetary Science Letters* 287, 77-85.

321 Georg, R.B., Halliday, A.N., Schauble, E.A., and Reynolds, B.C. (2007) Silicon in the

322 Earth's core. *Nature* 447, 1102-1106, doi:10.1038/nature05927.

323 Hammersley, J. (1996) *FIT2D V12.012 Reference Manual*. Eur. Synchrotron Radiat.  
324 Facil., Grenoble, France.

325 Hin, R.C., Fitoussi, C., Schmidt, M.W., and Bourdon, B. (2014) Experimental  
326 determination of the Si isotope fractionation factor between liquid metal and  
327 liquid silicate. *Earth and Planetary Science Letters* 387, 55-66.

328 Knibbe, J.S., and van Westrenen, W. (2018) The thermal evolution of Mercury's Fe-Si  
329 core. *Earth and Planetary Science Letters* 482, 147-159.

330 Komabayashi, T. (2014) Thermodynamics of melting relations in the system Fe-FeO at  
331 high pressure: Implications for oxygen in the Earth's core. *Journal of*  
332 *Geophysical Research* 119, DOI: 10.1002/2014JB010980.

333 Komabayashi, T., Fei, Y., Meng, Y., and Prakapenka, V. (2009) In-situ X-ray diffraction  
334 measurements of the  $\gamma$ - $\epsilon$  transition boundary of iron in an internally-heated  
335 diamond anvil cell. *Earth and Planetary Science Letters* 282, 252-257.

336 Komabayashi, T., Hirose, K., and Ohishi, Y. (2012) In situ X-ray diffraction  
337 measurements of the fcc-hcp phase transition boundary of an Fe-Ni alloy in an  
338 internally heated diamond anvil cell. *Physics and Chemistry of Minerals* 39,  
339 329-338.

340 Kubaschewski, O. (1993) in: Okamoto, H. (Ed.), Phase diagram of binary iron alloys.  
341 ASM International, Ohio, p. 380.

342 Kuwayama, Y., and Hirose, K. (2004) Phase relations in the system Fe-FeSi at 21 GPa.  
343 American Mineralogist 89, 273-276.

344 Li, J., and Agee, C.B. (1996) Geochemistry of mantle-core differentiation at high  
345 pressure. Nature 381, 686-689.

346 Lin, J.F., Heinz, D.L., Campbell, A.J., Devine, J.M., and Shen, G.Y. (2002) Iron-silicon  
347 alloy in Earth's core? Science 295, 313-315.

348 Lin, J.F., Scott, H.P., Fischer, R.A., Chang, Y.Y., Kantor, I., and Prakapenka, V.B. (2009)  
349 Phase relations of Fe-Si alloy in Earth's core. Geophysical Research Letters 36,  
350 L06306, doi:10.1029/2008GL036990.

351 Lister, J.R., and Buffett, B.A. (1995) The Strength and Efficiency of Thermal and  
352 Compositional Convection in the Geodynamo. Physics of the Earth and  
353 Planetary Interiors 91, 17-30.

354 Margot, J. L., Peale, S. J., Jurgens, R. F., Slade, M. A., and Holin, I. V. (2007) Large  
355 Longitude Libration of Mercury Reveals a Molten Core. Science 316, 710-714.

356 Mezouar, M., Giampaoli, R., Garbarino, G., Kantor, I., Dewaele, A., Weck, G., Boccato,  
357 S., Svitlyk, V., Rosa, A.D., Torchio, R., Mathon, O., Hignette, O., and Bauchau,

358 S. (2017) Methodology for in situ synchrotron X-ray studies in the laser-heated  
359 diamond anvil cell. *High Pressure Research* 37, 170-180.

360 Morard, G., Andrault, D., Guignot, N., Siebert, J., Garbarino, G., and Antonangeli, D.  
361 (2011) Melting of Fe-Ni-Si and Fe-Ni-S alloys at megabar pressures:  
362 implications for the core-mantle boundary temperature. *Physics and Chemistry*  
363 *of Minerals* 38, 767-776.

364 Ness, N.F. (1979) Magnetic-Fields of Mercury, Mars, and Moon. *Annual Review of*  
365 *Earth and Planetary Sciences* 7, 249-288.

366 Ozawa, H., Hirose, K., Mitome, M., Bando, Y., Sata, N., and Ohishi, Y. (2009)  
367 Experimental study of reaction between perovskite and molten iron to 146 GPa  
368 and implications for chemically distinct buoyant layer at the top of the core.  
369 *Physics and Chemistry of Minerals* 36, 355-363.

370 Ozawa, H., Hirose, K., Yonemitsu, K., and Ohishi, Y. (2016) High-pressure melting  
371 experiments on Fe-Si alloys and implications for silicon as a light element in the  
372 core. *Earth and Planetary Science Letters* 456, 47-54.

373 Rivoldini, A., Van Hoolst, Verhoeven, O., Mocquet, A., Dehant V. (2011) Geodesy  
374 constraints on the interior structure and composition of Mars. *Icarus* 213, 451–  
375 472.



376 Rubie, D.C., Frost, D.J., Mann, U., Asahara, Y., Nimmo, F., Tsuno, K., Kegler, P.,  
377 Holzheid, A., and Palme, H. (2011) Heterogeneous accretion, composition and  
378 core-mantle differentiation of the Earth. *Earth and Planetary Science Letters* 301,  
379 31-42.

380 Shahar, A., Hillgren, V.J., Young, E.D., Fei, Y.W., Macris, C.A., and Deng, L.W. (2011)  
381 High-temperature Si isotope fractionation between iron metal and silicate.  
382 *Geochimica et Cosmochimica Acta* 75, 7688-7697.

383 Siebert, J., Badro, J., Antonangeli, D., and Ryerson, F.J. (2013) Terrestrial Accretion  
384 Under Oxidizing Conditions. *Science* 339, 1194-1197.

385 Sohl, F., and Schubert, G. (2007) Interior structure, composition, and mineralogy of the  
386 terrestrial planets, in: Schubert, G. (Ed.), *Treatise on Geophysics*, pp. 27-68.

387 Sohl, F., and Spohn, T. (1997) The interior structure of Mars: Implications from SNC  
388 meteorites. *Journal of Geophysical Research-Planets* 102, 1613-1635.

389 Steinle-Neumann, G., Stixrude, L., Cohen, R.E., and Gülseren, O. (2001) Elasticity of  
390 iron at the temperature of the Earth's inner core. *Nature* 413, 57-60.

391 Stevenson, D.J., Spohn, T., and Schubert, G. (1983) Magnetism and Thermal Evolution  
392 of the Terrestrial Planets. *Icarus* 54, 466-489.

393 Takafuji, N., Hirose, K., Mitome, M., and Bando, Y. (2005) Solubilities of O and Si in

394 liquid iron in equilibrium with (Mg,Fe)SiO<sub>3</sub> perovskite and the light elements in  
395 the core. *Geophysical Research Letters* 32, L06313,  
396 doi:10.1029/2005GL022773.

397 Tateno, S., Kuwayama, Y., Hirose, K., and Ohishi, Y. (2015) The structure of Fe-Si alloy  
398 in Earth's inner core. *Earth and Planetary Science Letters* 418, 11-19.

399 Tsujino, N., Nishihara, Y., Nakajima, Y., Takahashi, E., Funakoshi, K., and Higo, Y.  
400 (2013) Equation of state of gamma-Fe: Reference density for planetary cores.  
401 *Earth and Planetary Science Letters* 375, 244-253.

402 Uchida, T., Wang, Y., Rivers, M.L., and Sutton, S.R. (2001) Stability field and thermal  
403 equation of state of  $\epsilon$ -iron determined by synchrotron X-ray diffraction in a  
404 multianvil apparatus. *Journal of Geophysical Research* 106, 21709-21810.

405 Wade, J., and Wood, B.J. (2005) Core formation and the oxidation state of the Earth.  
406 *Earth and Planetary Science Letters* 236, 78-95.

407 Wang, F.L., Tange, Y., Irifune, T., and Funakoshi, K. (2012) P-V-T equation of state of  
408 stishovite up to mid-lower mantle conditions. *Journal of Geophysical*  
409 *Research-Solid Earth* 117, B06209, doi:10.1029/2011JB009100.

410 Williams, J.P., and Nimmo, F. (2004) Thermal evolution of the Martian core:  
411 Implications for an early dynamo. *Geology* 32, 97-100.

412 Wood, B.J. (1993) Carbon in the core. Earth and Planetary Science Letters 117,  
413 593-607.

414 Yoder, C.F., Konopliv, A.S., Yuan, D.N., Standish, E.M., and Folkner, W.M. (2003)  
415 Fluid core size of mars from detection of the solar tide. Science 300, 299-303.

416 Zhang, D.Z., Jackson, J.M., Zhao, J.Y., Sturhahn, W., Alp, E.E., Hu, M.Y., Toellner, T.S.,  
417 Murphy, C.A., and Prakapenka, V.B. (2016) Temperature of Earth's core  
418 constrained from melting of Fe and Fe<sub>0.9</sub>Ni<sub>0.1</sub> at high pressures. Earth and  
419 Planetary Science Letters 447, 72-83.

420

421 Figure captions

422

423 Figure 1. Results of the experiments in (a) Fe-4Si and (b) Fe-6.5Si. The phases observed  
424 in XRD patterns are plotted: inversed triangle, hcp+bcc; square, hcp; normal triangle,  
425 fcc+hcp; circle, fcc. In (a), the boundaries between the fcc and hcp phases in pure iron  
426 (Komabayashi et al. 2009) and Fe-3.4Si (Asanuma et al. 2008) are also plotted. The data  
427 with asterisk have larger temperature uncertainty. In (b), our data are shown together  
428 with experimental data by Tateno et al. (2015). The typical uncertainty (2.5 GPa and  
429 200 K) is shown for a guide to the eye, see Table 1 for the uncertainty for each data  
430 point. The two datasets are fairly consistent considering the uncertainty in the laser  
431 heating experiments.

432

433 Figure 2. Series of XRD patterns collected in the run 2 for increasing temperature. The  
434 presence of the fcc phase was unambiguously marked by the appearance of (200) peak.

435

436 Figure 3. Temperature-composition diagram for the fcc-hcp transition. The open circle  
437 denotes the transition temperature in pure Fe (Komabayashi et al. 2009); the star  
438 symbols are the fcc-hcp reactions constrained by the present experiments; the filled  
439 circle is the P-T condition for a reaction of hcp = hcp + B2 phase observed in Tateno et

440 al. (2015). The stability fields of fcc+B2 and hcp+B2 were constrained by phase  
441 relations. In particular: (i) the boundary hcp = hcp+B2 should have a negative slope  
442 (Tateno et al. 2015) and (ii) the invariant boundary where the fcc, hcp, and B2 phases  
443 coexist should be placed at a temperature higher than the upper star at Fe-6.5Si.

444

445 Figure 4. The fcc-hcp boundaries in Fe-4Si and Fe-6.5Si (this study) with phase  
446 relations of pure iron (black lines) (Komabayashi et al. 2009; Komabayashi 2014).  
447 Thermal profiles of Mercurian and Martian cores in the system Fe-S are also shown  
448 (Tsujino et al. 2013).

**Table 1. Experimental conditions and results**

Run	P, GPa	T, K*	Phase	V(hcp), Å <sup>3</sup>	a (hcp), Å	c (hcp), Å	V(fcc), Å <sup>3</sup>	Remarks
<i>Fe-4Si (internal resistive heating)</i>								
1	16.4(6)	300	bcc+hcp	20.823(53)	2.4640(18)	3.9604(83)		
	13.1(4)	1060	fcc+hcp(small)	21.660(0)	2.4855(0)	4.04853(0)	43.643(14)	
	13.1(4)	1050	fcc				43.615(19)	
	13.1(4)	1080	fcc				43.683(19)	
2	23.6(4)	300	hcp	20.265(27)	2.4394(14)	3.9323(24)		
	22.6(4)	1120	hcp	20.816(3)	2.4554(2)	3.9866(3)		
	21.9(5)	1230	hcp+fcc	20.955(3)	2.4596(2)	3.9998(3)	42.352(0)	
	21.2(4)	1260	hcp+fcc	21.036(0)	2.4596(0)	4.0152(0)	42.343(38)	
	21.2	1260	hcp+fcc	-	-	-	42.330(5)	one peak for hcp
	21.2	1270	hcp+fcc	-	-	-	42.370(4)	one peak for hcp
	21.2	1330	fcc				42.475(15)	
	21.2	1360	fcc				42.520(12)	
	21.2	1430	fcc				42.720(21)	
	21.2	1450	fcc				42.854(69)	
3	33.3(2)	300	hcp	19.629(11)	2.4193(6)	3.8725(11)		
	32.7(5)	1030	hcp	20.016(10)	2.4280(5)	3.9206(10)		
	30.6(5)	1190	hcp	20.247(7)	2.4342(4)	3.9456(7)		
	30.2(5)	1240	hcp	20.312(9)	2.4361(5)	3.9521(9)		
	29.3(1.0)	1300**	hcp+fcc	20.411(13)	2.4399(7)	3.9592(13)	41.463(0)	
	29.3(1.1)	1370**	hcp+fcc	20.453(18)	2.4417(9)	3.9611(18)	41.392(0)	
	29.0(6)	1440	hcp+fcc	20.524(14)	2.4434(7)	3.9696(14)	41.285(0)	
	28.4(1)	1470	hcp+fcc	20.559(5)	2.4465(3)	3.9663(3)	41.344(51)	
	28.6(8)	1500	hcp+fcc	20.595(25)	2.4472(14)	3.9710(16)	41.480(37)	
	28.6	1580	fcc				41.652(23)	
	28.6	1620	fcc				41.650(19)	
4	41.0(5)	300	hcp	19.198(26)	2.3956(14)	3.8626(24)		
	43.7(6)	1130	hcp	19.392(13)	2.4019(7)	3.8813(12)		
	43.6(6)	1190	hcp	19.426(13)	2.4028(7)	3.8852(12)		
	43.3(6)	1250	hcp	19.473(10)	2.4043(5)	3.8899(9)		
	42.8(6)	1310	hcp	19.527(9)	2.4060(5)	3.8949(8)		
	42.3(5)	1380	hcp	19.592(7)	2.4081(4)	3.9011(6)		
	41.9(5)	1460	hcp	19.659(7)	2.4103(4)	3.9074(7)		
	41.8(7)	1410	hcp	19.637(14)	2.4106(8)	3.9021(13)		
	41.4(7)	1450	hcp	19.686(13)	2.4125(7)	3.9056(12)		
	41.5(7)	1560	hcp	19.736(13)	2.4139(7)	3.9111(12)		
	41.2(7)	1600	hcp	19.777(17)	2.4157(9)	3.9133(15)		
	41.5(8)	1680	hcp	19.799(25)	2.4158(13)	3.9173(23)		
	41.6(6)	1740	hcp+fcc	19.833(11)	2.4160(6)	3.9234(10)	39.934(0)	
	42.0(8)	1800	hcp+fcc	19.841(24)	2.4161(13)	3.9247(22)	40.055(0)	
	42.1(9)	1870	hcp+fcc	19.868(28)	2.4175(15)	3.9253(26)	40.080(0)	
	42.8(5)	1940	hcp+fcc	19.868(0)	2.4149(0)	3.9338(0)	40.133(10)	
	42.8	2050	fcc				40.204(13)	
	42.8	2090	fcc				40.216(36)	
	42.8	2160	fcc				40.315(44)	
42.8	2230	fcc				40.344(43)		
42.8	2260	fcc				40.340(48)		
5	46.0(3)	300	hcp	18.938(15)	2.3856(9)	3.8426(15)		
	50.0(6)	1050	hcp	19.020(12)	2.3882(7)	3.8507(11)		
	50.3(6)	1120	hcp	19.036(10)	2.3885(5)	3.8530(9)		
	50.6(5)	1230	hcp	19.068(7)	2.3890(4)	3.8579(6)		

	50.9(5)	1350	hcp	19.108(4)	2.3897(2)	3.8637(4)	
	52.0(5)	1530	hcp	19.124(5)	2.3901(3)	3.8657(5)	
	52.6(8)	1620	hcp	19.139(17)	2.3904(9)	3.8676(16)	
	52.8(1.3)	1750	hcp	19.186(44)	2.3914(24)	3.8739(41)	
6	75.8(1.2)	300	hcp	17.705(43)	2.3355(25)	3.7481(42)	
	70.1(1.6)	1080	hcp	18.135(48)	2.3563(22)	3.7716(72)	
	70.7(1.5)	1140	hcp	18.133(42)	2.3553(19)	3.7745(62)	
	70.8(1.3)	1200	hcp	18.151(35)	2.3551(16)	3.7789(53)	
	70.5(8)	1300	hcp	18.194(16)	2.3549(7)	3.7886(24)	
	68.7(7)	1460	hcp	18.323(10)	2.3596(5)	3.8000(16)	
	71.0(8)	1510	hcp	18.247(14)	2.3540(6)	3.8025(22)	
	71.0(1.0)	1650	hcp	18.301(21)	2.3552(8)	3.8096(36)	
	70.8(1.0)	1760	hcp	18.347(24)	2.3570(9)	3.8134(42)	
	70.6(1.1)	1840	hcp	18.387(25)	2.3585(9)	3.8169(43)	
	70.6(9)	1910	hcp	18.415(21)	2.3595(8)	3.8193(36)	
	71.2(9)	1960	hcp	18.410(17)	2.3600(8)	3.8169(26)	
	71.0(7)	2020	hcp	18.444(9)	2.3616(4)	3.8187(14)	
<b><i>Fe-6.5Si (laser heating)</i></b>							
1	24.0(1.3)	300	hcp	20.321(14)	2.4382(8)	3.9471(14)	
	28.8(2.3)	1320	hcp	20.539(10)	2.4438(5)	3.9713(9)	
	30.5(2.5)	1520	hcp	20.544(10)	2.4440(5)	3.9717(9)	
	29.6(2.4)	1500	hcp	20.602(9)	2.4457(5)	3.9773(8)	
	28.2(2.3)	1360	hcp	20.612(9)	2.4459(5)	3.9784(9)	
	28.0(2.3)	1430	hcp	20.671(9)	2.4473(3)	3.9854(12)	
	29.5(2.8)	1610	hcp	20.683(36)	2.4465(15)	3.9900(51)	
	29.5(3.1)	1640	hcp	20.695(60)	2.4507(25)	3.9788(82)	
	29.5(2.8)	1750	hcp	20.777(29)	2.4513(10)	3.9927(44)	
	29.5	1850	hcp+fcc	-	-	-	42.569(51) one peak for hcp
2	62.1(3.5)	300	hcp	18.308(55)	2.3616(21)	3.7904(93)	
	64.0(3.9)	1480	hcp	18.620(32)	2.3702(10)	3.8271(57)	
	64.0(3.7)	1600	hcp	18.664(20)	2.3702(6)	3.8364(37)	
	63.7(3.6)	1690	hcp	18.717(11)	2.3703(3)	3.8468(19)	
	66.0(5.3)	1930	hcp	18.711(77)	2.3733(8)	3.8360(157)	
	59.5(6.6)	2040	hcp	19.064(158)	2.3848(13)	3.8706(318)	
	53.0(3.5)	2140	hcp	19.456(0)	2.3960(0)	3.9134(0)	
	56.6(3.6)	2240	hcp	19.309(0)	2.3859(0)	3.9169(0)	
	56.6(3.6)	2340	fcc	-	-	-	39.548(156)

\* The uncertainty in temperature in the resistive and laser heating are typically 50 K and 10%, respectively.

\*\* Temperature uncertainty is as large as  $\pm 100$  K.

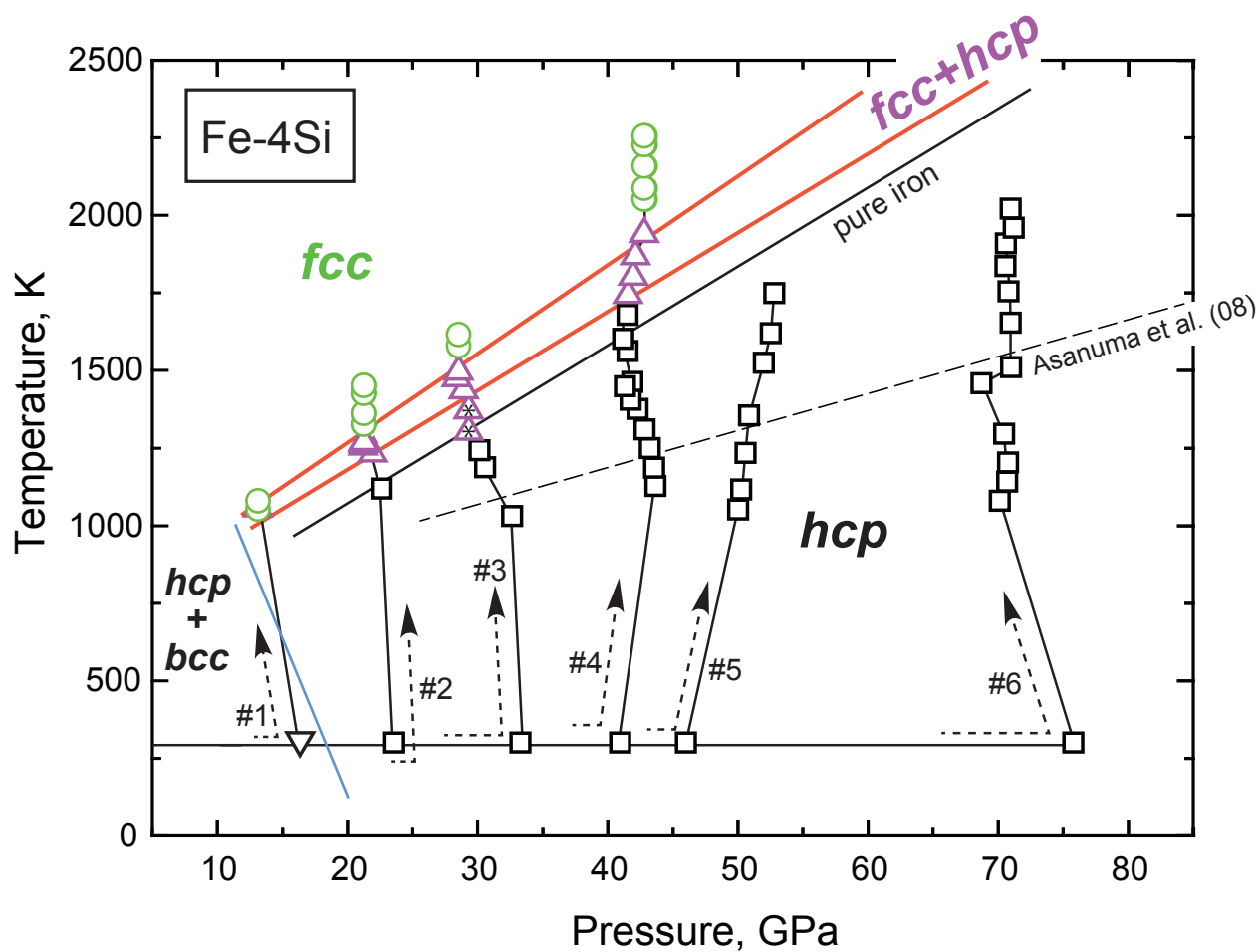
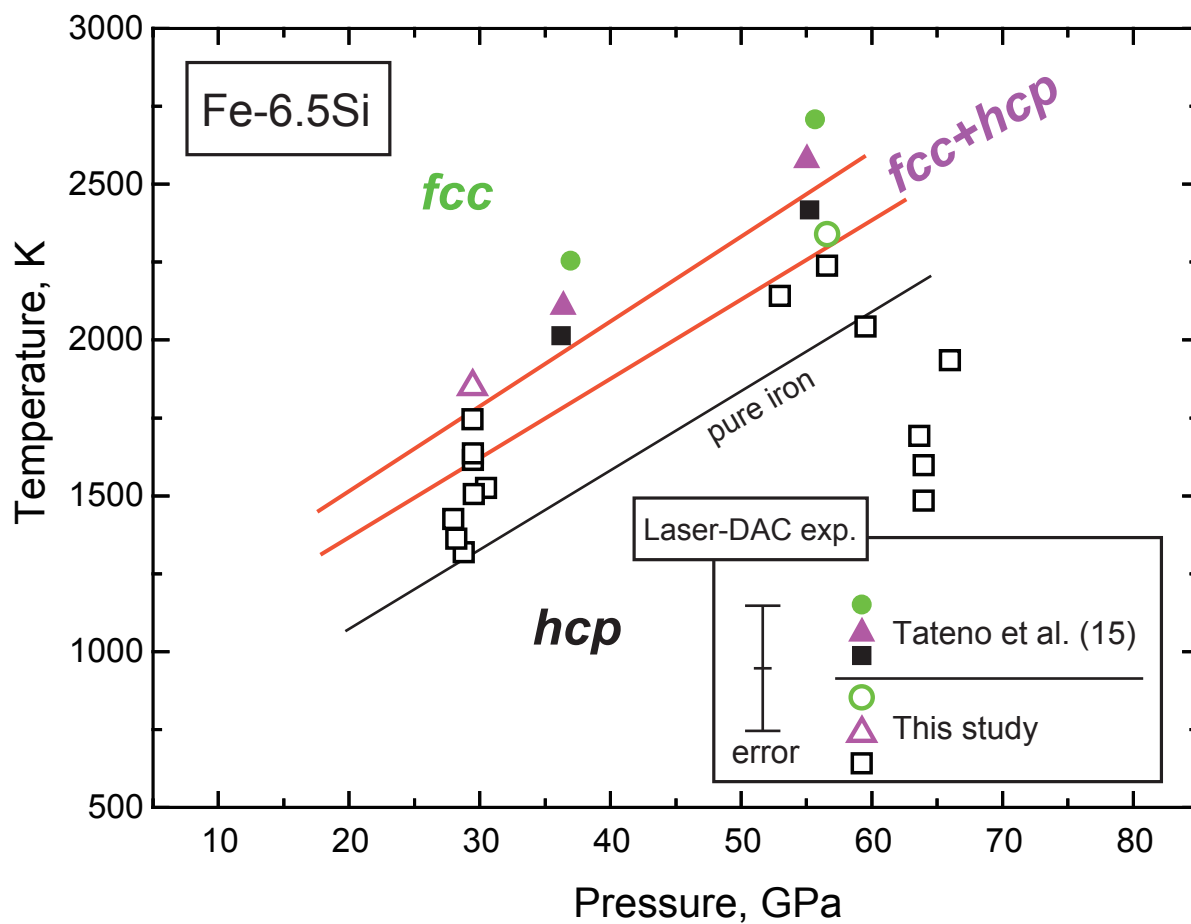
**a****b**

figure 1



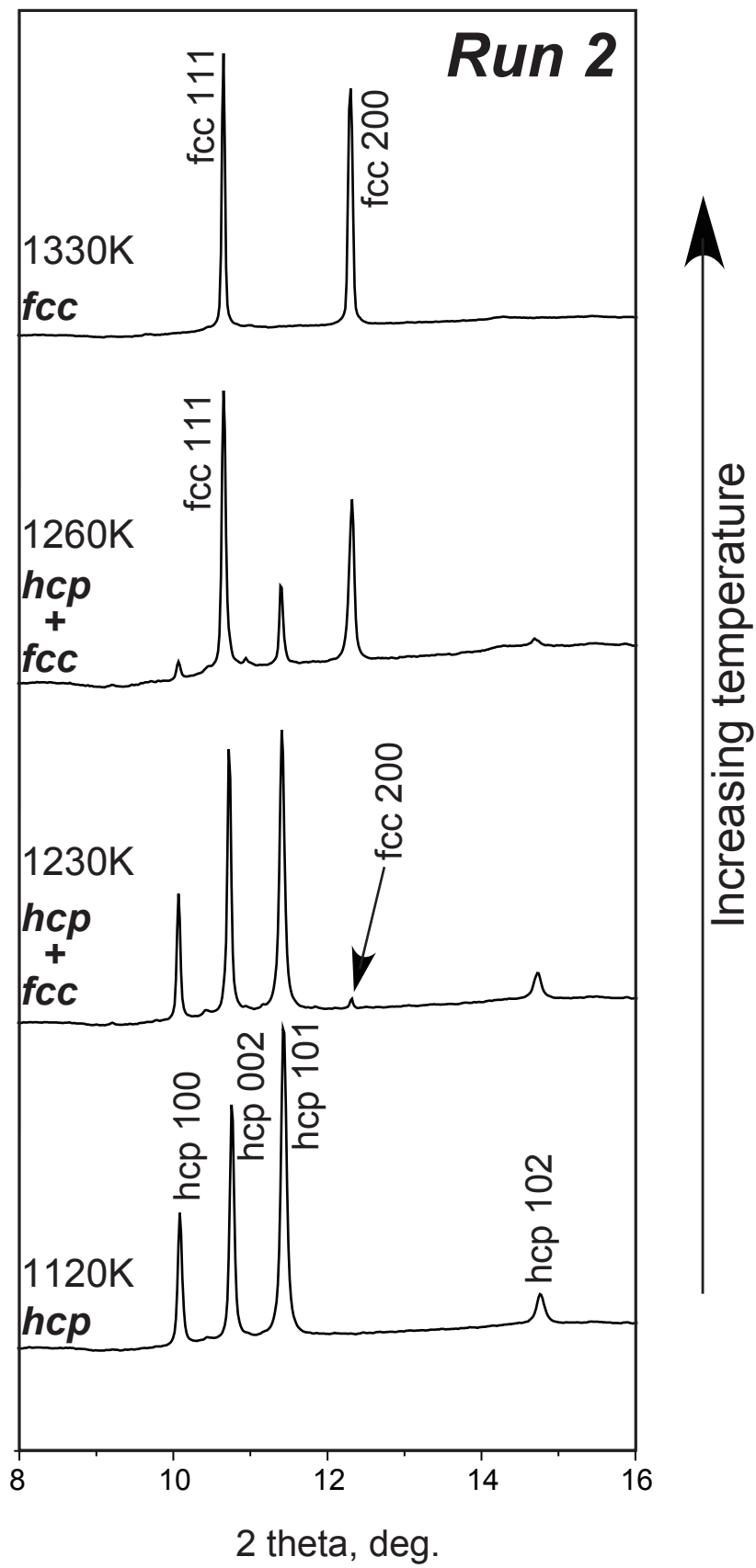


figure 2

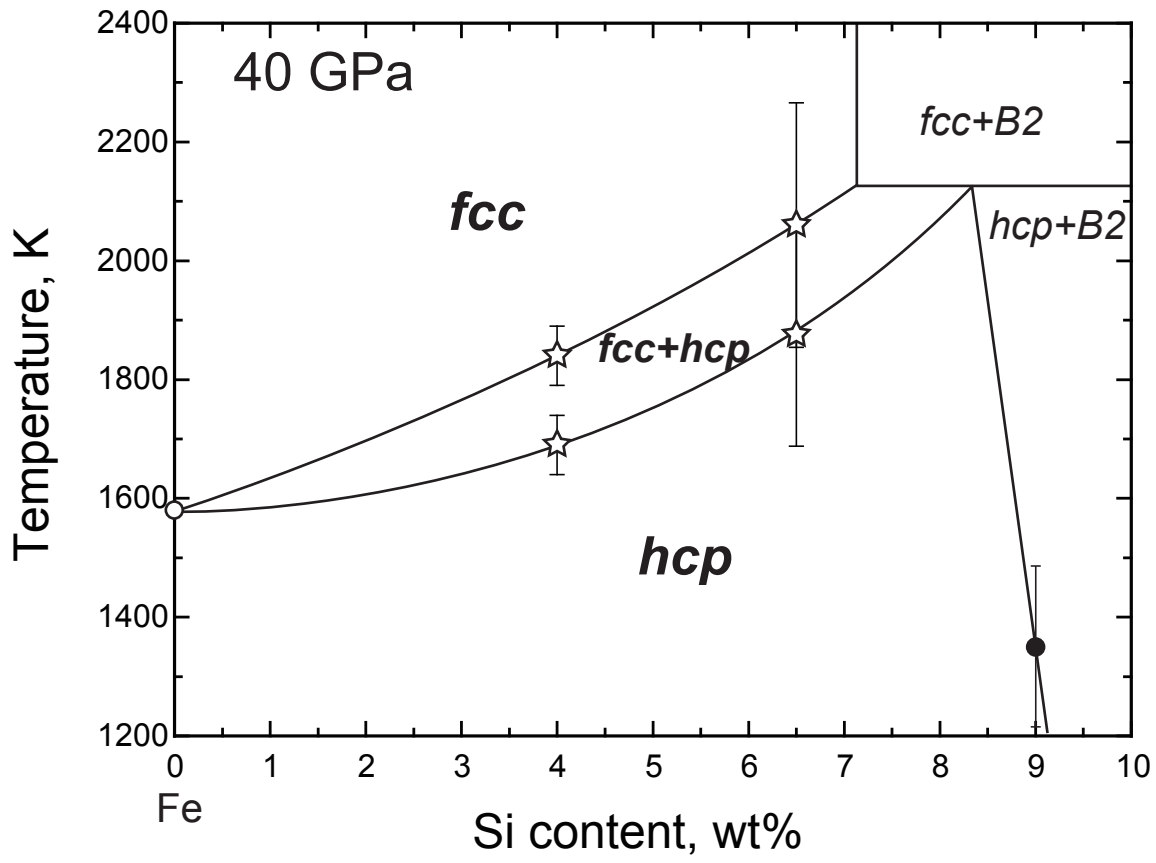


figure 3

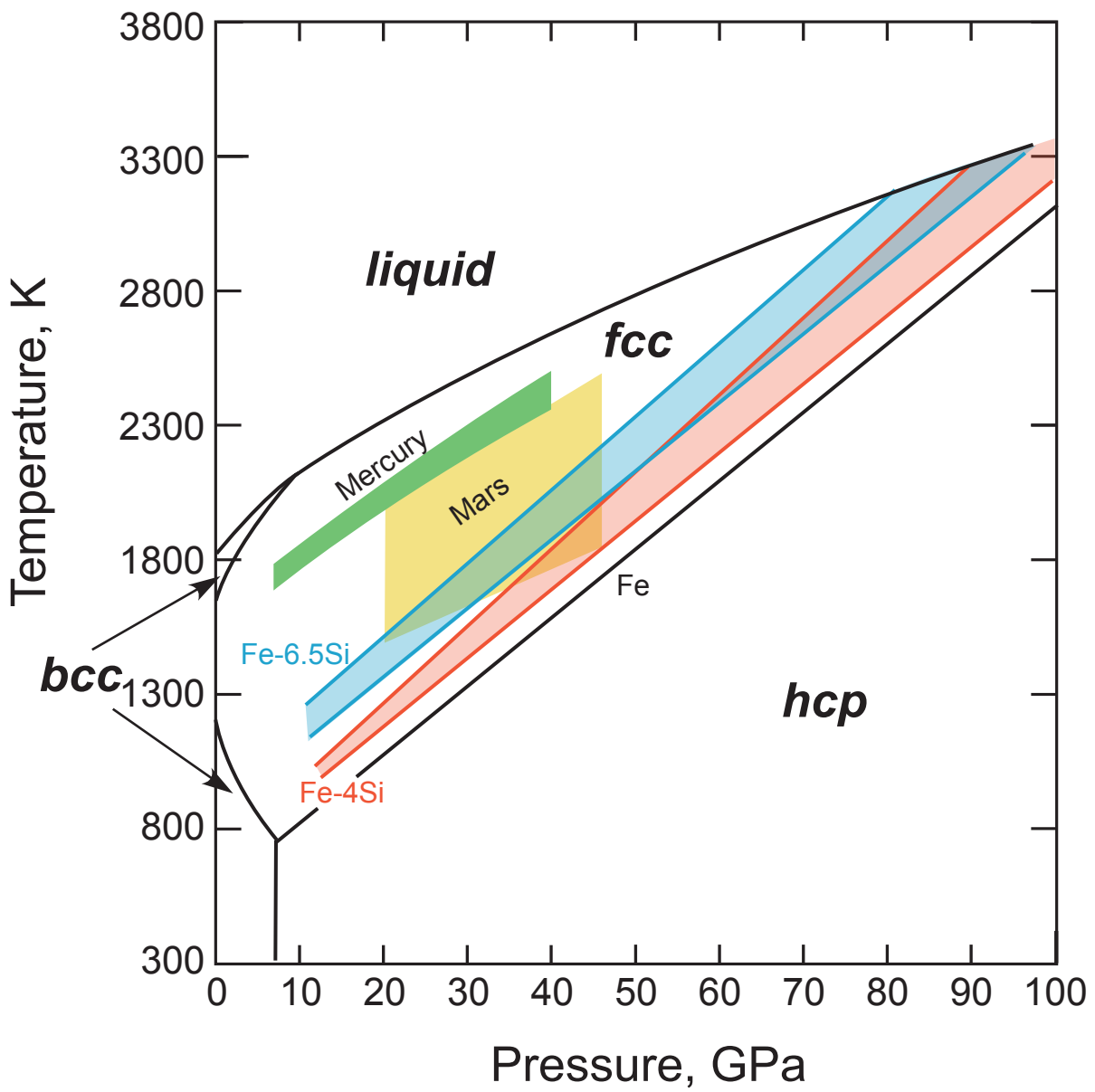


figure 4